Surface Science 667 (2018) 138–147

Contents lists available at ScienceDirect

Surface Science

journal homepage: www.elsevier.com/locate/susc

Surface chemical reactions induced on pyrite by ion bombardment

Gustavo Ruano[a,*], Fernando Pomiro[a], Julio Ferrón[a,b]

[a] Instituto de Física del Litoral (Universidad Nacional del Litoral - CONICET), Güemes 3450, Santa Fe 3000, Argentina
[b] Departamento de Materiales, Facultad de Ingeniería Química, Universidad Nacional del Litoral, Santiago del Estero 2829, Santa Fe 3000, Argentina

ARTICLE INFO

Keywords:
FeS_2
XPS
Helium bombardment
Pyrite
Factor analysis

ABSTRACT

Through X-ray photoemission spectroscopy (XPS), we studied the chemical changes induced in a natural crystal of pyrite (FeS_2) upon exposure to 4.5 keV He^+ beam. We found an important reducing effect induced by ion bombardment leading to the production of iron embedded in the pyrite matrix. Through a combination of the usual Doniach–Sunjic treatment and Factor Analysis of XPS yields, we were able of analyzing the full Fe 2p XPS signal. We could in this way distinguish Fe compounds with the same binding energy for the Fe $2p_{3/2}$ yield.

Our results show that He^+ bombardment disrupts the ionic environment producing S_2^{-2} and S^0, Fe^{2+} and Fe^{3+} ions, and the reduction to metallic iron. The remaining pyrite matrix does not passivate the embedded iron structures, which are readily oxidized under air exposure. The oxide formed resembled that of magnetite from the XPS point of view. Further He^+ bombardment proved to be efficient to reduce the iron oxide back to iron again.

© 2017 Elsevier B.V. All rights reserved.

1. Introduction

The impact of energetic ions on the surfaces of airless bodies immersed in the outer space (SW: solar wind) is the responsible for the final aspect of their surfaces. While isolated impacts are able of producing the breaking of chemical bonds, leading to the creation of new molecules, the final elemental composition of the surface is determined by the SW sustained bombardment giving place to surface sputtering and implantation [1,2]. Chemical and physical processes that reduce sulfur minerals can lead to amazing consequences and some of them have been even related to the origin of life [3]. These alterations have been determined either by optical measurements made at distance [4] or by direct inspection of the outer samples. Within this last group we can find, for instance, the lunar soil brought to our planet, [5,6] and the impact of pyrite containing asteroids [7]. The other remaining possibility of gaining information about the solar wind effects rests on space condition simulations in the laboratory. Since outer space vacuum conditions, as well as solar wind ones, are easily obtained nowadays in any surface laboratory, these kinds of experiments can be routinely performed. Thus, several irradiation experiments on minerals surfaces have been published showing, for instance, the reduction of Fe^{2+} to metallic iron by energetic H^+ and He^+ bombardment [6,8].

The alteration of matter by ion bombardment is, on the other hand, a branch of material science currently of enormous interest, with the most recent applications involving nanomaterials development and graphene production [9]. In a recent work [10,11] we studied the diffusion mechanisms governing the CuN nanostructures formation in Cu(100) under keV N^+ ion bombardment [12,13]. The ion induced reduction of pyrite is then of interest from condensed matter physics and an astrophysical points of view. So far, with the same experimental setup, involving ion implantation and sputtering under solar wind and airless surface environment, we can gain knowledge about the mechanisms of nanostructure formation under ion bombardment, and the microscopic mechanisms of metal reduction and surface segregation determining the final aspects of astrophysical bodies.

The first step to achieve our goals is the selection of an adequate substrate. In this sense, we chose pyrite (FeS_2) for several reasons: *i)* it is a naturally inexpensive abundant mineral; *ii)* it is diamagnetic and semiconductor in its native form; *iii)* an industrial commodity in the production of iron and sulfuric acid; *iv)* it is matter of study in basic science in a broad spectrum of topics, ranging from primordial biochemistry [3,14,15] to nanometric semiconductors development; [16] *v)* from the astrophysical point of view, the presence of pyrite in meteorites has been traced back to the planet mars; it has been even linked to the possible existence of water and volcanic activity in the earlier stages of mars formation and to the controversial discovery of fossilized microorganisms in the famous asteroid ALH84001 [7].

Pyrite is sensitive to low energy electron irradiation [17] and it is known that ion bombardment produces preferential sputtering leading to S vacancies [18,19]. Additionally, early in the 70s the chemical effect of Ar^+ irradiation on many iron-sulfur compounds was assessed using X-ray photoemission spectroscopy (XPS) [20]. The “old” problem of

* Corresponding author.
E-mail address: gustavo.ruano@ifis.santafe-conicet.gov.ar (G. Ruano).

https://doi.org/10.1016/j.susc.2017.10.009
Received 31 July 2017; Received in revised form 5 October 2017; Accepted 10 October 2017
Available online 16 October 2017
0039-6028/© 2017 Elsevier B.V. All rights reserved.

Table 1
Parameters obtained from the DS fitting for the experimental XPS data and the FA obtained basis.

Samp.	S 2p				Fe $2p_{3/2}$				
	Comp.	Gauss.width [eV]	Lorenz. width [eV]	BE [eV]	Comp.	Gauss. width [eV]	Lorenz. width [eV]	Asym.	BE [eV]
Fe0						1.26		0.48	706.96
FeS_2 (DS)	S1 ($S_2^{2-}{}_{bulk}$)	0.99	0.15	162.53	F1 ($Fe^{2+}{}_{bulk}$)	0.82	0.2	0	707.09
	S2 ($S_2^{2-}{}_{detached.}$)	1.65		161.95	F2 (Fe^{0})	1.26		0.48	706.98
	S3 ($S^{2-}{}_{surf.}$)	1.25		160.96	F3 ($Fe^{2+/3+}{}_{surf.}$)	3.17		0	709.57
FeS_2 (FA)	A1 ($S_2^{2-}{}_{bulk}$)	1.18	0.15	162.5					
	A2 ($S_2^{2-}{}_{detached}$)	1.75		161.88					
	A3 ($S^{2-}{}_{surf.}$)	1.65		161.30					

determining the effect of the interaction of the pyrite with low energy ions is still a topic of interest in the pyrite research community, given that ion irradiation is a common procedure for obtaining atomically and clean ordered samples [21].

In this work, we studied the chemical changes induced in a natural crystal of pyrite (FeS_2) upon exposure to 4.5 keV He^+ beam. XPS results into a very convenient technique to study this system, due to its chemical sensitivity and since no X-ray beam damage has been observed during the measurement process. Through a combination of the usual Doniach–Sunjic treatment of XPS yields and Factor Analysis, we were able of analyzing the full Fe 2p XPS signal. We propose a coherent model to explain of ongoing surface reactions during the interactions of the He ions with the pyrite surface.

2. Experimental

2.1. Samples

A pyrite sample of 1 × 1 × 0.1 cm was produced by cutting a thin slice out of a natural cube of the mineral provided by Stanford Minerals mined in Rioja Spain. The fragment was chosen to be flat, shiny and uniform. The usual surface cleaning procedure of rinsing the sample in isopropanol was performed. Any surface cleaning procedure based on ion bombardment and surface annealing was avoided, since we are just interested in the ion induced reduction of the sample.

Magnetite nanoparticles were produced via the well know method of reduction of iron(III) acetylacetonate with borohydride [22] by the team FENTON in INGAR and kept immersed in isopropanol to prevent air oxidation. Maghemite formation upon air exposure produces the loss of their magnetic characteristics. On the other hand, aggregated macroparticles in solution exhibited a very clear response under a magnetic field.

2.2. X-ray photoemission spectroscopy

XPS measurements were surveyed in a commercial XPS spectrometer VG inside an ultra-high vacuum (UHV) chamber with a base pressure of 1×10^{-9} mbar. The spectra were recorded with a hemispherical electrostatic energy analyzer (r = 10 cm) and Al K Alpha X-ray radiation (1486.6 eV). A beam of 4.5 keV He^+ ions was used, impinging in an angle of 60° referred to the normal surface. The impacted area on the sample was approximately 1 cm^2 affecting the whole sample. The ion beam current density was probed with a Faraday cup and was kept constant along the experiment at 5.5 μA/cm^2. The accumulated ion dose at the end of the experiment (64 min) was 1.3×10^{17} ions/cm^2. Slight charging of the surface was observed, shifting the peaks without affecting their lineshapes. The charge condition was monitored and later corrected, as usual, by determining the position C 1s peak in every spectrum.

As the goal of this work is the study of the ion induced reduction of pyrite, we checked in first place if the sample undergoes any degradation process under X-ray bombardment. In doing that, we took continuous XPS spectra along 8 h, where we did not notice any lineshape changes either in Fe or in S yield, confirming in this way that photon beam damage can be neglected.

2.3. Doniach–Sunjic algorithm

To analyze the chemical change in the pyrite surface, in first place we used the standard fitting technique for XPS spectra; a Doniach–Sunjic (DS) algorithm, [23] preconditioned (as usual) with a fixed Lorentzian width of 0.20 and 0.15 eV for Fe and S lineshape respectively and a Shirley-like background subtraction. For further details on the implementation of the algorithms refer to the SI.

2.4. Fe $2p_{3/2}$

The lineshape of the Fe $2p_{3/2}$ photoemission signal presents challenges for its analysis due to its complexity arising from peak asymmetries, complex multiplet splitting, shake-up and plasmon loss structures [24]. This is particularly true in the case of metallic iron; as it is widely documented the lineshape of this line is dominated by multiplet splitting generated during the photoemission process given the resulting photoion has several possible final state configurations (hence many energies). The resulting spectrum is an asymmetric wedge-like line. On the other hand, for iron compounds, such as pyrite, where the iron is in 2+ oxidation state the lineshape of this signal is very different. For pyrite the signal is dominated by a symmetric peak with (Fe^{2+} low-spin in the bulk) and a satellite corresponding to $Fe^{2+/3+}$ multiplets in the surface [25].

We performed the fitting of an atomically clean surface of metallic Fe (99.9%) to obtain the lineshape of this compound. The obtained parameters are shown in Table 1. In the fitting of the pyrite data set we included the metallic Fe component (F2) obtained above and we let free the intensity and position to minimize the χ square but remaining the shape defining parameters fixed i.e. Gaussian width and asymmetry. In a similar fashion we obtained the Gaussian width for the symmetric component corresponding to unaltered pyrite (F1 in Fig. 1(a)) and used this value to fit the rest of the set. The less intense components were accounted with a single symmetric lineshape with non-restricted Gaussian width, position or intensity.

2.5. S 2p doublet

We fitted the set of spectra in the S 2p region using a predefined lineshape that takes into consideration the 1:2 ration in the intensities of S $2p_{1/2}$ to S $2p_{3/2}$ and a fixed (1.18 eV) spin orbit splitting (SOS) for the symmetric doublet components. From the unaltered pyrite we obtained the Gaussian width of the main doublet S1, in the same way, this parameter and the relative binding energy (respect to the S1 component) of the additional doublets (S2 and S3) were obtained using the spectrum in which they were maximum (Fig. 1(c) right panel). Those values where kept fix in the fitting of the rest of the set.

2.6. Factor analysis

To analyze the XPS spectra of the doublets S 2p and Fe 2p we applied the FA method, which serves to identify the presence of different chemical species. The first step in FA [26] is the determination of the minimum number of linearly independent factors required to describe the

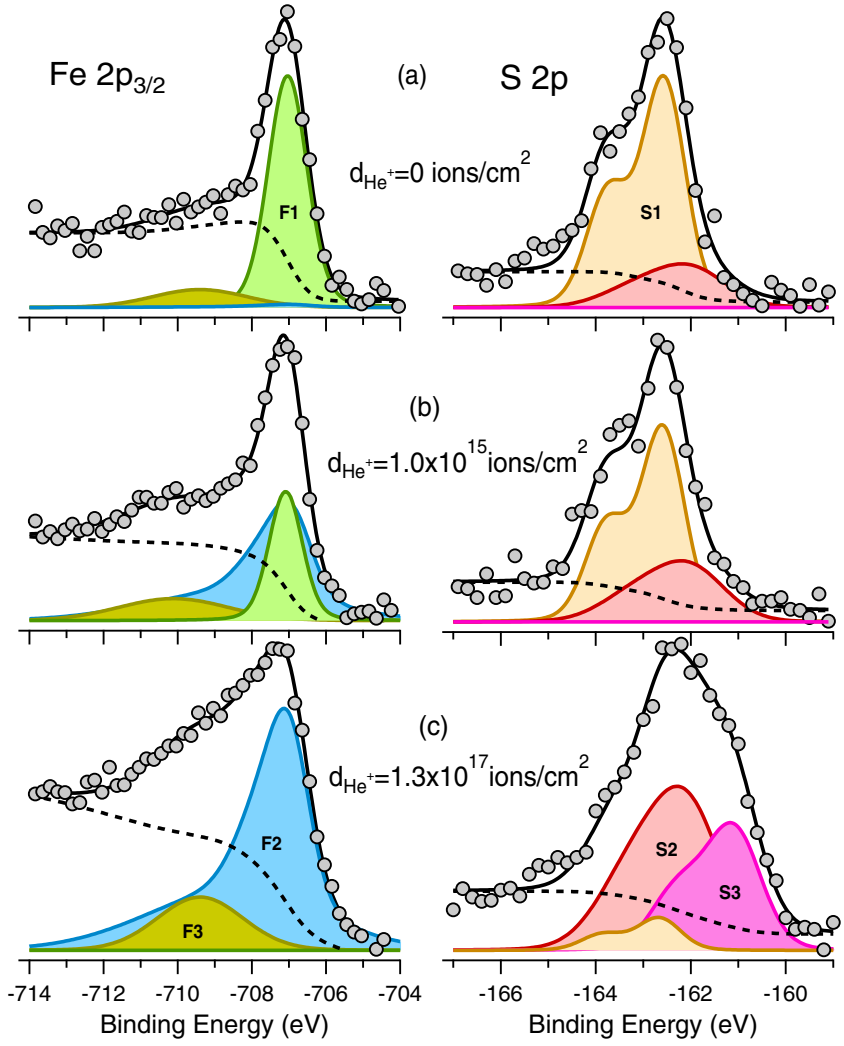

Fig. 1. Selected series of XPS Fe $2p_{3/2}$ (left column) and S 2p (right column) spectra of a natural pyrite surface reflecting the effect of an increasing dose of He^+ 4.5 keV. The best DS fit of each spectrum is illustrated by the curve (full line) which intersects the data points (gray full dots). F1: Fe^{2+} bulk peak, F2: metallic Fe peak, F3: Fe^{2+} and Fe^{3+} surface peak. S1: S_2^{2-} bulk peak, S2: S_2^{2-} surface peak and S3: S^{2-}. The dotted line curve is the Shirley background. (For interpretation of the references to color in this figure legend, the reader is referred to the web version of this article.)

complete series of spectra corresponding to the evolution under study. In doing that, we compare the experimental error with the error performed in reproducing the experimental data with a minimum set of factors. This procedure is performed as electron emission spectra are added sequentially, and each time this error surpasses the experimental error a new factor appears in the process. Once the number of independent factors is known, the shape of the contribution coming from each mechanism (base) is determined through a least square fit procedure called Target Transformation (TT). For further details refer to the SI.

3. Results and discussion

The work in ultra-high vacuum conditions in surface characterization is closely associated to the atomically clean surface concept. In this way, the cleaning process is usually associated to ion sputtering and annealing cycles. Within this context, the pyrite surface cleaning is based in low energy He^+ or Ar^+ bombardment and rather low temperature (~600 K) annealing cycles [21,27]. However, since we are just interested on the effect on the surface of the ion-substrate interaction, we are compelled to avoid any physical cleaning procedure. Thus, we limited ourselves to use only a soft chemical cleaning with ethanol to degrease the surface.

The wide XPS scan, depicted in Fig. S1 in Supplementary Information, reveals the presence of iron and sulfur, and rather high amounts of C and O, as it is usual with materials coming from atmospheric pressure environment. XPS studies of vacuum-fractured pyrite surfaces and those reacted with atmospheric gases and aqueous solutions demonstrate that for surfaces subjected to oxidation, the presence of the oxidizing agent is not enough to alter the Fe 2p and S 2p photoemission lineshapes [28–34]. These studies show that accumulation of oxygen containing species at mineral surfaces does not necessarily indicate oxidation of Fe or S, or formation of Fe–O and S–O chemical species.

In order to characterize in a correct way the initial sate of our pyrite sample, we collected XPS Fe 2p and S 2p spectra before the He^+ bombardment process (Fig. 1(a)). The Fe $2p_{3/2}$ spectrum (left panel) displays a strong, near-symmetric peak centered at ~707 eV, and a wedge-shaped tail extending to ~711 eV. The Fe signal is remarkably similar to the measurement performed in other laboratories for vacuum-fractured pyrite surfaces [30,35,25]. While the strong, near-symmetric peak at ~707 eV represents the octahedral coordinated (O_h symmetry) Fe^{2+} contribution from bulk sites of pyrite (F1 component), [28,30,34,35] the high binding energy tail of the spectrum is composed primarily of Fe^{2+} and Fe^{3+} surface state contributions (F3 component) [25].

Since all valence electrons of Fe^{2+} on bulk sites are paired (low-spin configuration and diamagnetic behavior), a single singlet photo-peak

should appear (~707 eV). However, the broken symmetry of Fe^{2+} located at surfaces, edges and corners split the *d* orbital energies, allowing a promotion of d_{xy} electrons to the $d_z{}^2$ orbitals. This promotion turns the Fe^{2+} cations located at surfaces into paramagnetic (intermediate or high spin configuration), resulting in multiplet splitting of their associated photopeaks. [25] The Fe^{3+} surface state is, on the other hand, necessarily paramagnetic and its photoemission peaks are in the same way multiply split. Although we can identify two components (F1 and F3 in Fig. 1(a)), our energy resolution is not enough to discriminate all multiplets contained in the lower intensity component F3. As complicated as the Fe 2p structure in the pyrite may be, there is no chance to confuse any of these peaks with Fe oxide states. In fact, Fe–O surface states are centered close to 710–712 eV, [36] and clearly no such surface states are detected in any of our spectra, along all the bombarding process. We can then conclude that Fe is un-oxidized in the starting pyrite sample, and it is not oxidized in the UHV chamber during all the experiment, neither by the residual oxygen, nor by the possible existence of knock on implanted oxygen.

The S 2p spectrum shown in the right panel of Fig. 1(a) was collected simultaneously with the Fe 2p one. The spectrum shows two distinct doublet contributions. The most intense one (~162.5 eV) represents the contribution of S atoms of S–S dimmers (disulfide $S_2{}^{2-}$) residing on bulk sites of pyrite (S1 component). [35,37] In pyrite structure, each S atom is tetrahedrally coordinated, bonded to another S atom and three Fe^{2+} to produce S–S dimers. The effect of the surface, edges and corners is reflected in the sulfur case by the appearance of a shifted peak located at ~161.8 eV (S2 component). [25] The S spectrum in vacuum-cleaved pyrite surfaces shows also a third component, associated to the monosulfide specie (S^{2-}). [25,30,35] In the cleaved surfaces, this species is generated by the fracture of the S-S bond in the disulfide anion, and so it is reasonably absent in our natural pyrite surface. However, it indeed appears once the bombarded is initiated (S3 along right column in Fig. 1). On the other hand, there is no traces of S–O compounds (165–168 eV region) [33] hence there is neither sulfur oxidation on the starting pyrite surface, nor along the bombarding process, coherently with the iron results.

In Fig. 1 we display a selected set of XPS Fe $2p_{3/2}$ (left column) and S 2p (right column) spectra reflecting the effect of an increasing dose of He^+ 4.5 keV bombardment, showing a typical bombarding evolution. The displayed exposure times, were chosen in a potential series; i.e 30s, 60s,.....3840s and the accumulated He^+ dose at the end of the experiment was 1.3×10^{17} ions/cm^2. The changes in the lineshapes of both signals show evidence of important alterations in the chemical composition of the pyrite surface. Thus, the initially well-defined S 2p doublet broadens; increasing the signal at lower binding energies, and the Fe $2p_{3/2}$ undergoes a notable increase of the high binding energy tail.

It is apparent that He^+ bombardment rapidly disrupts the chemical environment of the iron and sulfur atoms i. e. 2 min (or 4.1×10^{15} ions/cm^2) are enough to clearly see the appearance of monosulfide S^{2-} signal (S3) and metallic Fe (F2) (see Fig. 2). The final composition of the film is characterized by mostly metallic Fe (F2) with S in a mixture of mono (S3) and detached disulfide (S2), but with only a bit disulfide signal coming from non-altered original tetrahedral sites (S1).

To start with a quantitative analysis of the evolution of Fe and S compounds we used the standard DS fitting technique. In Fig. 2 we display quantitatively the relative amount evolution of each component of Fe (Fig. 2(a)) and S (Fig. 2(b)) 2p signals, obtained using the DS algorithm, as a function of the accumulated He^+ dose. The continuous rupture of Fe^{2+}–$S_2{}^{2-}$ bonds is evidenced by the drop down of the Fe^{2+} and $S_2{}^{2-}$ bulk relative amount, F1 and S1 respectively. This latter is accompanied by the increase of the relative amount of the S2 (uncoordinated or detached $S_2{}^{2-}$ on the surface) and the coming out of the F2 (metallic Fe) and S3 (monosulfide S^{2-}) signals. The variation in the F3 component is clearly smaller than the others ones. As it can be observed in Fig. 2(a), Fe rapidly changes its oxidation state from Fe^{2+} in FeS_2 to Fe^0 and this occurs together with the grow up of S2 and S3 contribution for sulfur (Fig. 2(b)). At the end of the process less than 10% of the original compounds are preserved as it was shown in Fig. 1(c).

To explain the relative amount evolution of the different species, in particular the arising of metallic iron; we may consider the transference of the pair of electrons from the detached $S_2{}^{2-}$ anion to the detached Fe^{2+} cation on the pyrite surface and the consequent formation of two S^0 atoms and metallic Fe, according with the reaction:

$$S^{2-}_{2\,(\mathrm{detached})} + Fe^{2+}{}_{(\mathrm{detached})} \rightarrow Fe^{0}{}_{(\mathrm{sup.})} + 2S^0 \quad (1)$$

To understand this process is necessary to point out that the He+ bombardment generates an increase of the detached Fe^{2+} (F3 component) and $S_2{}^{2-}$ (S2 component) at the surface. In the case of iron, this increase is not observed in Fig. 2(a). The reason of this is that almost all the extra detached Fe^{2+} ions generated by the bombardment are reduced to Fe^0 (F2 component) in the pyrite surface as it is proposed in Eq. (1). The case of sulfur is different, firstly because initially there is more sulfur than iron in the pyrite surface and secondly because there is another process (Eq. (3)) that generates detached $S_2{}^{2-}$ (S2 component) anions as the bombardment proceeds, as we will see below.

Regarding to the S^0 species postulated in Eq. (1), since the vapor pressure of elemental S^0 is very high, the species may sublimate from bombarded pyrite in the UHV environment or, in turn, react with a subtending disulfide ($S_2{}^{2-}$, signal S2 in Fig. 1) to produce polysulfide ($S_3{}^{2-}$) in the near surface [7,35]. We did not observe the presence of these polysulfides. In the equations we indicate with the subscript "detached" the species that constitute the pyrite surface (i. e. Fe^{2+} and $S_2{}^{2-}$ uncoordinated in the surface) and the subscript "surf." is used for the species that are generated in the surface by the bombardment (i. e. Fe^0 and S^{2-}).

It is known that the ion S^-, originated during the homolytic dissociation of the anion $S_2{}^{2-}$, is very unstable [35] and that it recombines quickly according to the following possible kinetics:

$$2S^- \rightarrow S^0 + S^{2-}_{(\mathrm{surf.})}(\mathrm{S3}) \quad (2)$$

$$2\,S^- \rightarrow S^{2-}_{2\,(\mathrm{detached})}(\mathrm{S2}) \quad (3)$$

$$Fe^{2+}_{(\mathrm{detached})}(\mathrm{F3}) + S^- \rightarrow Fe^{3+}{}_{\mathrm{surf.}}(\mathrm{F3}) + S^{2-}_{(\mathrm{surf.})}(\mathrm{S3}) \quad (4)$$

The process, as described in Fig. 2, appears initially ruled by the reaction described by Eq. (1), with the production (and sublimation/surface reaction) of elemental S^0, driving the kinetics towards the metallic Fe production. At this very first stage S2 component (surface $S_2{}^{-2}$ anion) increases its concentration at the expense of S1 one (Eq. (3)) and a shortly afterwards we observe a growth in the intensity of the S3 component (S^{-2} yield). The growth rate for the initial stage ($0 <$ dose $< 4.1 \times 10^{15}$ ions/cm^2) for both components is roughly the same, indicating that the reactions in Eqs. (2), (3) and (4) proceed with similar kinetics. As the bombardment continues ($4.1 \times 10^{15} <$ dose $< 6.2 \times 10^{16}$ ions/cm^2) S3 growth stagnates and the process is dominated by an accelerated production of S2. In this intermediate regime the reaction in Eq. (3) prevails. With the progression of the damage of the crystalline structure (dose $> 6.2 \times 10^{16}$ ions/cm^2), and the appearance of stronger dipoles, the mechanism described by Eqs. (2) and (3) becomes less likely, i.e. saturation of the S2 signal occurs over time. Thus, the occurrence of two S^- turns to be less likely, moving the process to a kinetics dominated by Eq. (4). The correlation between S1 and F1 suggest that both $S_2{}^{2-}$ and Fe^{2+} become in a similar fashion, giving evidence that Eq. (1) describes the main overall evolution but, at the same time, there is not the only active process. There is a point in the evolution of F1 and S1 in Fig. 2 that deserves to be discussed a bit more. If the process is governed by Eq. (1) the disappearance of F1 and S1 should be in phase. However, in Fig. 2 we can see a faster fall down of the component related to Fe than the S one. This result may be easily rationalized by taking into account the escape depth of photoelectron. Due to its higher energy S photoelectrons escape (3.2 nm) is 50% larger than those corresponding to Fe electrons, (2.2 nm) [38]. On

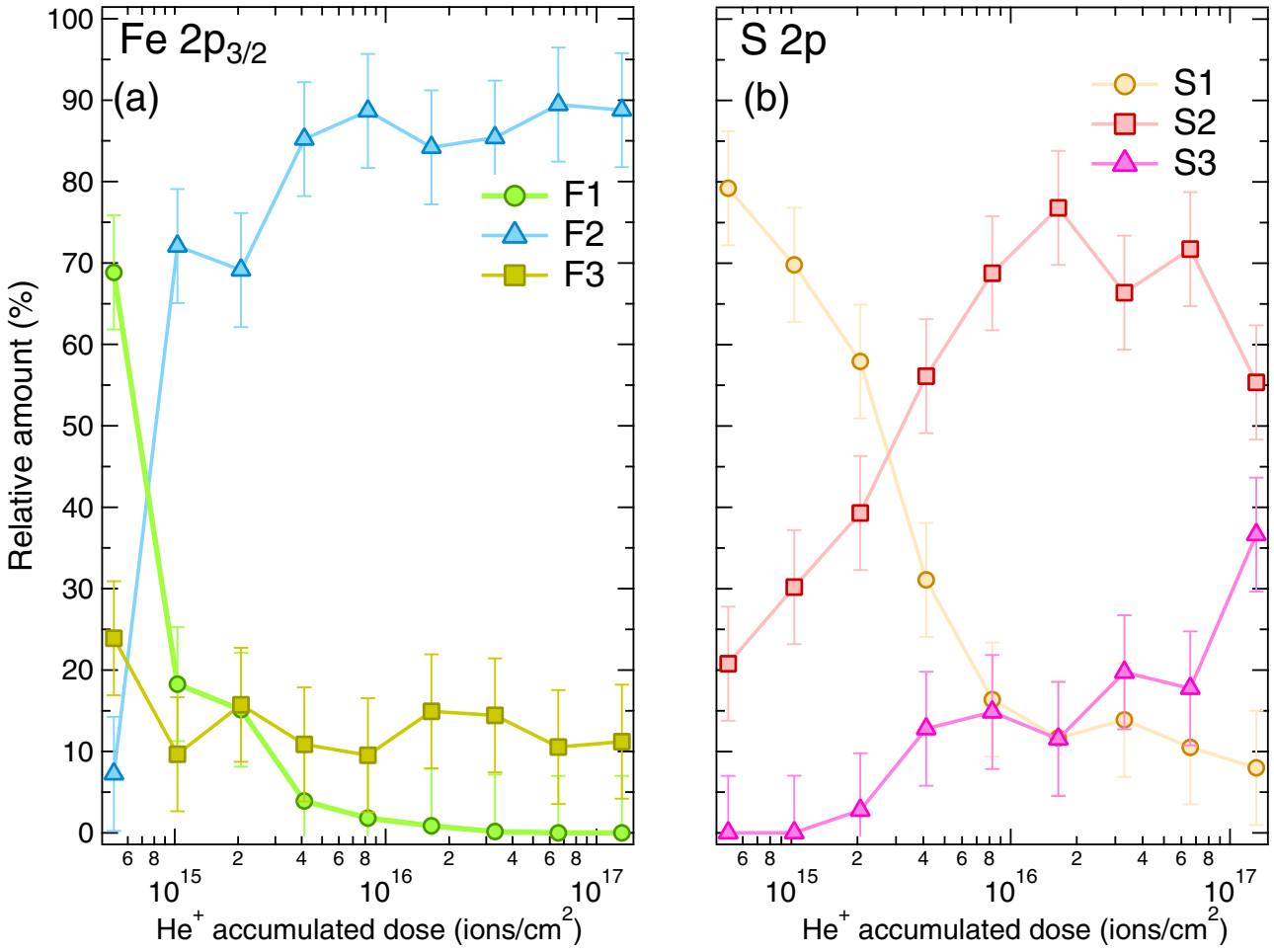

Fig. 2. Relative amount evolution of each component of the Fe (a) and S (b) 2p signals obtained using the DS algorithm as a function of the accumulated He^+ dose.

the other hand, the in-depth extent of the alterations is limited by the range of the He ions that was estimated around 30 nm [39]. Thus, if we are sampling the substrate deeper with S than with Fe, it is completely reasonable that Fe reaches its final value before.

Regardless of the differential sampling depth and non-uniformity of the changes that could explain the difference in the evolution of the coordinated species (F1 and S1), our model foresees, in Eqs. (1) and (2), a diminution in the ratio evolution of S to Fe. This is consistent with the well known preferential sputtering of S [19]. In Fig. 3 the intensity ratio S/Fe obtained from the DS fitting as a function of the irradiation time is shown. The downwards trend matches approximately the evolution of the F1 species, as seen in Fig. 3, which suggests an important role of the mechanism proposed in Eq. (1) in which F1 (atomic S) is a reactant (product).

The reduction of Fe ionic species in the pyrite matrix to give place to metallic iron is undoubtedly demonstrated by our experiments based on XPS BE and yield shape measurements. However, when we try to quantify the amount of metallic iron formed in the ion bombardment process, the point turns to be a bit more obscure. The first problem appears, as we already mentioned, due to the different escape depth of Fe 2p and S 2p photoelectrons that leads to the sensing of different volumes. However, neglecting this fact, we could say that in Fig. 3 the S/Fe ratio decreases in a way compatible with the formation of FeS_x, with x near to 1, like troilite (FeS) or the intemediate pyrrhotite (FeS_{1+x} with $0 < x < 1$). There are additional arguments against assigning the reduction of pyrite process to mainly the formation of these sulfur deficient species. A comparison among different iron sulfides using XPS has being performed by Thomas et.al. [40], finding that for troilite or

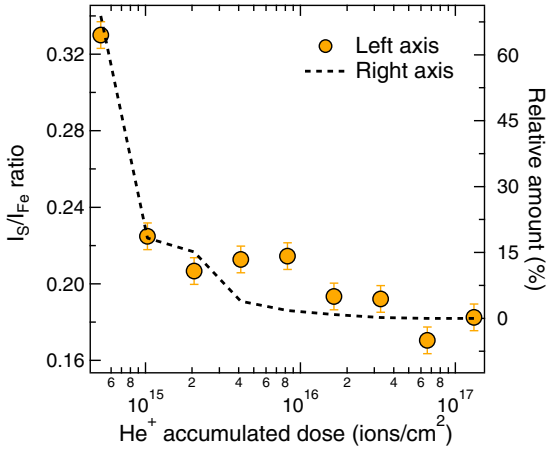

Fig. 3. Intensity ratio S/Fe (dots-left axis) and relative amount of the Fe^{2+} bulk (F1) (dashed line-right axis) obtained from the DS fitting as a function of the accumulated He^+ dose.

pyrrhotite the Fe $2p_{3/2}$ signal is dominated by the high-spin contributions (Fe^{2+}/Fe^{3+}) in the form of multiplets (709–710 eV), and the S 2p signal by the monosulfide (S^{2-}) (160–162 eV). The presence of S^{2-} is then a necessary marker of the troilite or pyrrhotite formation. However, although during the first stages, depicted in Figs. 1 and 2, a broadening of the Fe $2p_{3/2}$ signal takes place, no S^{2-} (S3) is observed at all. This backs to our assumption that metallic iron is formed. As the irradiation

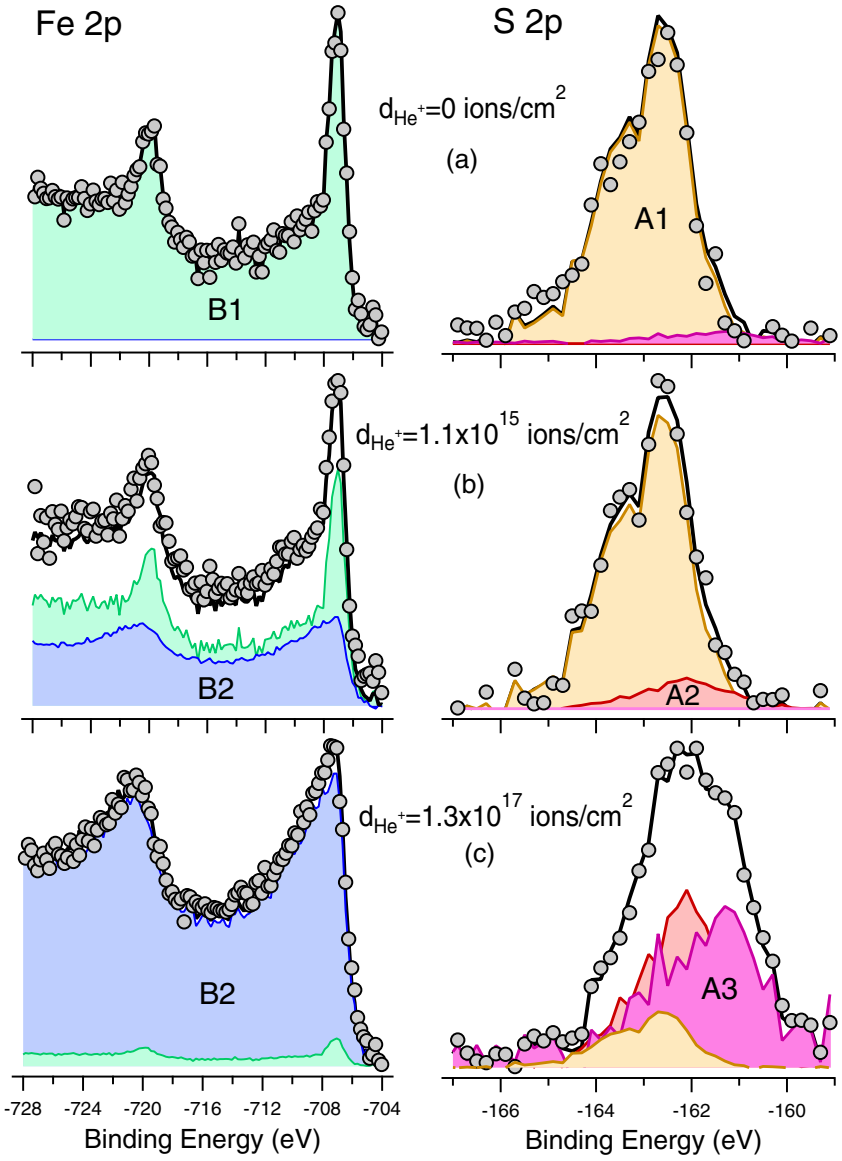

Fig. 4. XPS lineshapes (Fe 2p: B1 and B2; S 2p: A1, A2 and A3) obtained through FA for the same points shown in Fig. 1.

proceeds (t > 60 s) both the requirements (Fe^{2+} high-spin species and S^{2-}) for the formation of pyrrhotite/troilite are met. Therefore, there might be some minor amount of Fe belonging to troilite or pyrrhotite domains, we are assigning to unbounded or to metallic iron. The upper limit for this species can be established at 15%, taking into account the high-spin Fe^{2+} species (assuming all the high spin components are associated to the formation of either pyrrhotite or troilite) at the end of the evolution. This value could be a realistic bound to the formation of the sulfur deficient species.

Up to this point we have presented and discussed our results under the light of the most standard deconvolution technique, the DS algorithm. This methodology is a powerful tool to gain insight on both the chemical state and the relative composition of the surface in particular counting with a priori knowledge base on the system. However, there are some difficulties that are worthy to point out. In the first place, in our best knowledge, the usual approach in the DS deconvolution for the Fe 2p signal in pyrite only the 3/2 component of the doublet, as in the first part of our analysis, has been taking into consideration. There is useful information obtainable from the fitting of the whole doublet, such as the energy of the spin-orbit splitting (SOS). For instance this feature has been used as a part of the characterization of different species during the formation of iron nanoparticles. [41] There are, however, practical reasons that hindered the fitting of the whole Fe 2p doublet, such as the introduction of some additional parameters necessary to take into consideration differences in the lineshape of the signals in the doublet. In that regard, in this study, as the bombardment proceeds it may originate new Fe species with different lineshapes according to their different photoemission features i.e. initial and final state effects. In an effort to retrieve any missing information we complement our data treatment and analysis with Factor Analysis, a technique that proved useful in dealing with signals that evolves with time [26].

The powerful of FA algorithm [26] is to allow us finding the minimum number of linearly independent spectra (bases) needed to reproduce the full set of data. Based in the Function Indicator [26] analysis we found, for the same case (He^+ 4.5 keV) studied up to here, three linearly independent bases for the S 2p and two for the Fe 2p signals evolution. In Fig. 4 we show the FA results for the XPS lineshape and for the same points as in Fig. 1, but applied for the full 2p ($2p_{1/2}$ and $2p_{3/2}$) spectrum in the case of Fe.

It is important to remark here that FA, in contrast with DS analysis, uses the whole set of spectra, along the full ion bombardment process (while DS fits each spectrum at a time), and it does not require neither

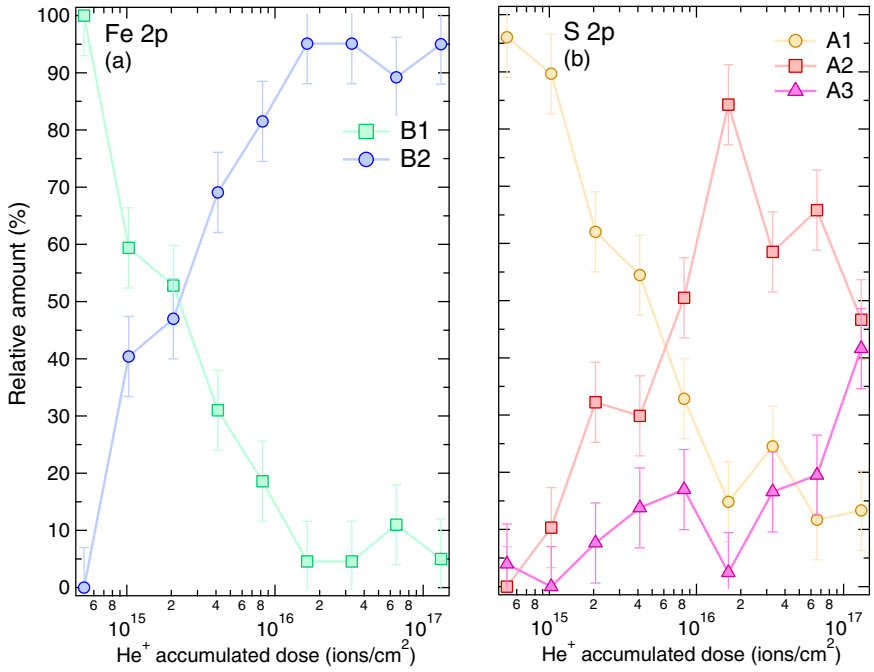

Fig. 5. Relative amount evolution of each component of the Fe (a) and S (b) 2p signals obtained using the FA algorithm as a function of the accumulated He^+ dose.

preconditions nor predefined lineshapes to start with. In other words, FA does not require the previous knowledge of the shape and position of XPS yields, allowing us to obtain both these results just by using only the experimental yields. On the other hand, this is the reason of the noisy aspect and poorer definition of these lineshapes, when compared to DS results. Despite this fact, the reproduction of the experimental results is remarkable good (see full line in Fig. 4).

In Fig. 5 we display the weight evolution of each component of Fe (a) and S (b) 2p signals obtained using the FA algorithm, as a function of the bombardment time.

With both results at hand, DS and FA, we can validate our first analysis. We observe that for the case of S 2p the results offered by both techniques are in good agreement. In Table I we summarize not only the parameters that define the lineshape of the raw spectra but also those resulting of fitting the bases obtained by FA for S 2p. With such a consistency it is not surprising that the evolution of the relative quantities, shown in Fig. 5(b), matches quite well to those in Fig. 2(b). For the case of Fe 2p the connection between the results is not as straightforward as for S; to begin with only a couple of linearly independent basis (B1 and B2) are needed to describe the full evolution. However, despite the fact that FA found only 2 components for iron signal against the three ones needed for the DS fitting, the general trend is preserved.

The fact that FA does not detect a third component for Fe, as revealed by DS analysis, is just in the roots of this method. While FA searches for a minimum number of bases to reproduce all the experiment, in using DS fitting we can change the shape of the functions (broad and energy location of the function) for each spectrum, since we fit them independently. A smooth increase of the broad of experimental spectra, for instance, would be treated by FA as the appearance of as many bases as spectra are in the experiment. The missing FA base, the non-resolved multiple peaked spin states, has, according to DS analysis (Fig. 2(a)), a rather constant distribution along the experiment. In the FA evolution, this absence is traduced in a slight difference in the detailed kinetics of the transformation i.e. the time in which the main species reach the same weight is 70 s for FA and around 30 s for DS.

In Fig. 6, the bases (B1 and B2) obtained by FA for the Fe 2p evolutions are shown. The first one is composed by a couple of dominant structures with narrow binding energy widths. This basis clearly represents the doublet Fe $2p_{3/2}$ –Fe $2p_{1/2}$ at 707.0 eV and 719.8 eV respectively. In Fig. 5(a) we see that the initial weight for this basis is 100% and therefore identical to it. The second basis B2 comprises two strong asymmetric peaks at around 707.1 eV and 720.4 eV. Like in the case of B1, we noticed that B2 is almost identical to the last spectrum of the evolution.

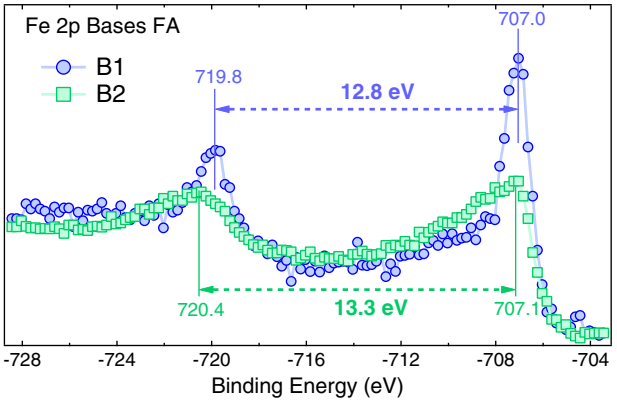

Fig. 6. Basis B1 and B2 obtained by FA for the Fe2p doublet evolution. The black dashed line corresponds to the Fe 2p signal of the metallic iron XPS spectrum. The horizontal dashed lines denoted the SOS for each bases. (For interpretation of the references to color in this figure legend, the reader is referred to the web version of this article.)

The goal of this part of the work will come from the detailed analysis of the B1 and B2 shape. The Fe $2p_{3/2}$ binding energies for pyrite and metallic iron are practically indistinguishable [32,42]. Thus, being the difference in the energy position between Fe $2p_{3/2}$ for B1 and B2 peaks lower than our experimental uncertainty (0.2 eV), we could not draw any conclusion from the energy shifts, as it is the power of XPS. However, the key information in this case is related to the spin-orbit splitting. Thus, although no relevant information coming from the positions of the Fe $2p_{3/2}$ peaks in B1 and B2 can be obtained, as it is shown for direct comparison in Fig. 6 we can certainly ensure that the SOS in B2 strongly resembles that of metallic iron (dashed line in Fig. 6) [42]. Thus, this result further validates our original supposition of metallic

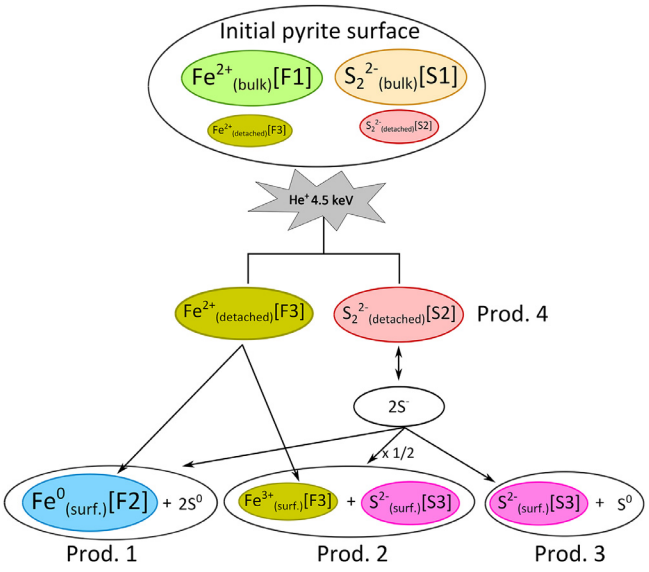

Scheme 1. Graphical summary of the probable chemical reactions taking place during pyrite surface He^+ bombardment.

iron formation and justifies the introduction of its lineshape parameters in the DS analysis.

To summarize and clarify the possible pathways of pyrite decomposition during or right after the He^+ irradiation, we depict in Scheme 1 the possible mechanisms for spontaneous S^- relaxation proposed by Nesbitt (Eqs. (2)–(4)) [35]. In the same scheme we also include energy assisted processes that can take place during the irradiation, i.e. the dissociation of the coordinated ionic species in the near surface region schematized as a spark in the cartoon. It seems to be an accepted assumption that energetic ion breaks both, the strong (Fe^{2+}–S_2^{2-}) and weaker bonds in the molecular anion (S—S^{2-}). This first stage is confirmed by our observations that the extinction of F1 (and B1) and the rise of S2 (and A2) follow approximately complementary kinetics (Figs. 2 and 5). Following the evolution of Fe^{2+}, it can be either reduced (product 1 in Scheme 1) in an assisted process, or be further oxidized producing also S^{2-} (S3) (product 2 in Scheme 1). Our observations indicate that the S3 component does not change significantly during the first minutes of irradiation, but the iron signal associated to F2 rapidly climbs up, indicating that the first stage is dominated by the kinetics producing metallic iron and S2 (product 4 in Scheme 1).

During ion bombardment of pyrite, S vacancies are produced due to preferential sputtering [19]. Regarding the evolution of the unstable S^- species, there are many possible different mechanisms; but the only one than describes the strong build-up of S2 component is the formation of isolated molecular anions (product 4 in Scheme 1). On the other hand, the S3 component associated with S^{2-} starts to climb up upon the saturation of the S2 component. One simple way to explain this is to consider the molecular anion as an intermediate in the formation of S^{2-}, the population of S^- and S_2^{2-} reaches a steady state favoring the conversion to S^{2-} and a neutral S^0 (product 3 in Scheme 1). Although our resolution is not good enough to separate the individual contributions of Fe^{2+} and Fe^{3+} from the metallic iron, comparison between B2 and the Fe reference sample, along with the DS fitting shown in Fig. 2(c), indicates that the multiplets of uncoordinated cationic species are a component of the base. In this regard, the variation in the S3 species in BE and width (as shown in Table I) may be attributed, in the beginning of the evolution, to the existence of the precursor Fe^{2+} and in the end to the existence of some Fe^{3+} (product 2 in Scheme 1).

Using XPS, supported by Factor Analysis, we have developed a model of the formation of different sulfur and iron compounds during the He ion bombardment process. Although the model actually fit the experimental results, and the generation of Fe^0 is reasonable demonstrated, we have independent additional experiments that help us to confirm the actual metallic Fe generation. Based in the fact that while iron oxidizes rapidly in dry air, pyrite is rather inert at the same conditions, [32] we designed and performed an (oxidation) experiment to obtain additional support to our model.

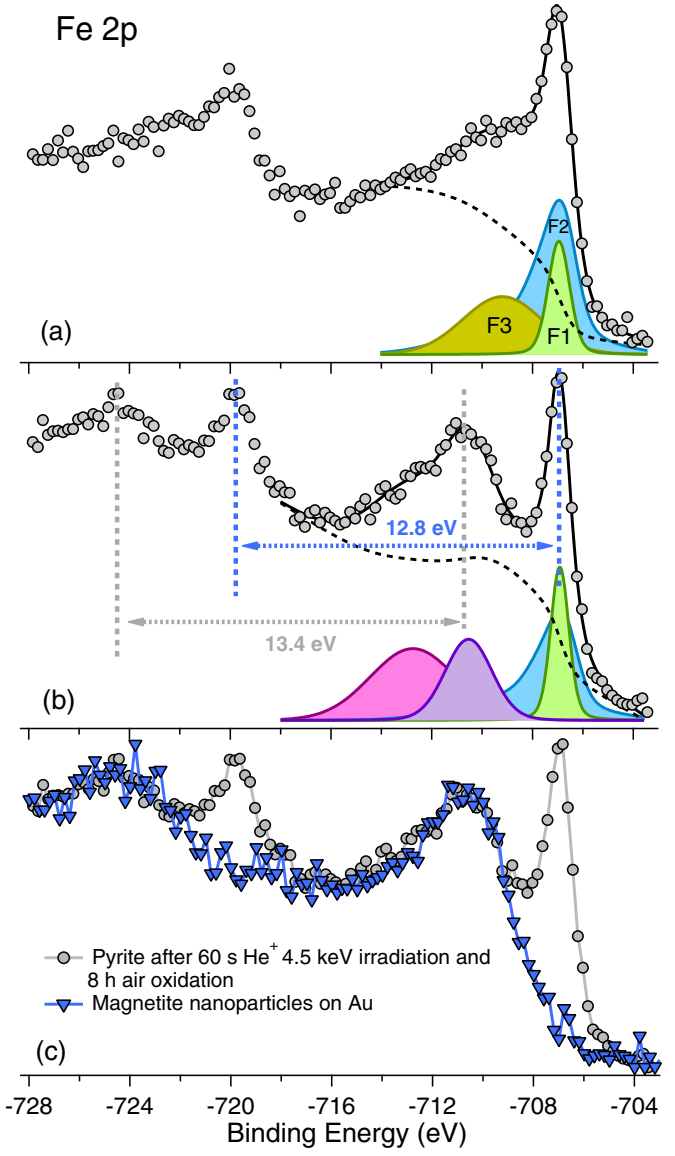

Fig. 7. Fe 2p XPS spectra of pyrite: (a) after 60 s of He^+ irradiation (b) followed by 8 h of air oxidation. The best DS fit of the Fe $2p_{3/2}$ peak obtained in each spectrum is illustrated by the curve (full line) which intersects the data points (gray full dots). The dotted line curve is the Shirley background. (c) Fe 2p XPS spectra of pyrite after 60 s of He^+ irradiation followed by 8 h of air oxidation compared with the magnetite one. (For interpretation of the references to color in this figure legend, the reader is referred to the web version of this article.)

Our starting sample was pyrite altered by ion bombardment in a way as to obtain similar quantities of sulfur species; S^{2-}, FeS_2*, and iron species; Fe*S_2 and Fe^0. This condition is achieved by bombarding the sample during 60 s. After the bombardment, we extracted it from the UHV chamber and left it during 8 hours in dry air at atmospheric pressure. In Fig. 7 we depict the XPS spectra for the bombarded (a) and post oxidized (b) samples. We also included the spectrum corresponding to magnetite nanoparticles (c) as a reference. The He^+ bombardment produces, as it was already discussed, the broadening of the Fe 2p lineshape.

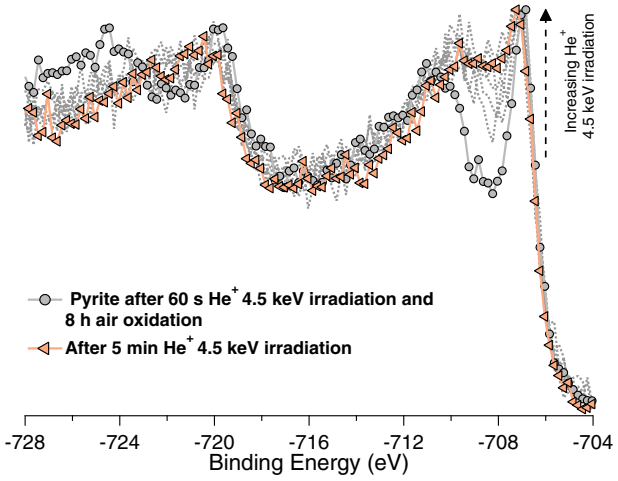

Fig. 8. Comparison of the He^+ bombarded and oxidized Fe 2p XPS spectra in pyrite and its evolution upon He^+ irradiation. In dotted gray lines, some intermediate spectra of the evolution are shown. (For interpretation of the references to color in this figure legend, the reader is referred to the web version of this article.)

A DS fitting of the Fe $2p_{3/2}$ spectrum shows three signals with the same lineshape of those in Fig. 1, with an F3 component centered around 709.2 eV with a width of 3.6 eV. After the oxidation process, this lineshape changes from the characteristic broaden signal to a more definite one, with prominent broad peaks (2 and 4 eV) around 710.5 and 712.4 eV respectively. The SOS for these new doublets is 13.4 eV. Taking into consideration the relative intensity of the signals arising of this analysis we conclude that while the fraction of F1 component variation can be neglected (0.22–0.18), the metallic Fe (F2) halved (0.39–0.2) and the entire non-coordinated species (F3) fraction prior to the oxidation (0.39) disappeared.

The new doublets represent a fraction of 0.62 of the total signal after the oxidation in Fig. 7(b). Laveneur et al [41]. obtained a very similar lineshape for Fe 2p using high-resolution XPS for oxidized nanoparticles embedded in SiO_2. The authors associate the main Fe $2p_{3/2}$ peak at 710.8 eV to magnetite (Fe_3O_4) forming a shell around the nanoparticles (in the interface SiO_2 Nps–Fe) and the signals at higher binding energy (near 712.6 eV) to "shake up" peaks characteristic of ions Fe^{+3} and Fe^{+2}. In order to provide a direct comparison, we ourselves performed XPS measurements on magnetite nanoparticles deposited on a gold substrate. In Fig. 7(c) we show the comparison of both these lineshapes, i.e. Fe 2p from bombarded and post-oxidized pyrite and magnetite nanoparticles (scaled), supporting the idea that the XPS peaks appearing after the oxidation process of bombarded pyrite corresponds actually to iron oxide.

The results, summarized in Fig. 7, provide strong evidence supporting our initial ideas, i.e. *i)* the low reactivity of pyrite (F1), *ii)* the high reactivity of metallic iron (half of F2 component oxidized) and *iii)* the total chemical combination with oxygen of the detached $Fe^{2+/3+}$. Thus, we can reasonably ensure that He^+ bombardment generates metallic iron, and that this iron is oxidized after air exposure. Although the XPS lineshape of this oxidized iron largely agrees with that of magnetite nanoparticles (Fig. 7(c)), we cannot of course claim that we are obtaining neither magnetite nor nanoparticles. It is also clear, on the other hand, that these results do not exclude this possibility, and encourage us to continue with these experiments. Thus, microscopic measurements i.e. STM and MFM, surface local density of states and elemental in-depth distribution to gain insight about this point are underway. Another interesting result here is that we have shown that the pyrite matrix does not preclude completely the oxidation of the formed iron. Thus, in case we want to maintain the reduced iron as metallic, we will need to think in a passivizing coating film.

As a final confirmation of the Fe^{x+} reducing role of the He^+ bombardment, i.e. it is not restricted to the pyrite case; we irradiated the reduced and post oxidized pyrite (bombarded pyrite in Fig. 7 (a) and (b)). The evolution of Fe 2p yield, shown in Fig. 8, resembles that in Fig. 1, the narrow peak at 711 eV of binding energy, we associated to magnetite, rapidly (5 min of irradiation) evolves into the broad asymmetric structure of iron imbedded in pyrite. Thus, the final state of iron seems to be the same, either one starts with pyrite or magnetite. The He^+ bombardment leads to the re-appearance of metallic iron. Although the sputtering of iron oxide, as a whole, could explain this result, the low sputtering yield of Fe under He bombardment lead us to think that a similar mechanism for the FeS_2 may be also playing a role in the reduction of the magnetite back to iron.

4. Conclusions

We present results about the reduction process of natural single crystal pyrite under 4.5 keV helium ion bombardments. We found that energetic He^+- pyrite interaction gives place to iron reduction and the appearance of monosulfide. We found that the application of DS analysis together with FA can be a powerful technique to identify elements, when changes in BE and broadening occurs simultaneously. We propose a model based in the disruption of the ionic environment producing ions S_2^{-2} and S detached from Fe^{2+}, as well as $Fe^{3+}$and Fe^0. Through a post oxidation experiment we found support to our model. Unfortunately, we also found that the pyrite matrix does not passivate the embedded iron structures, that are readily oxidized to a magnetite like (from the XPS point of view) iron oxide.

Acknowledgments

We wish to thank Dr. Ernesto Martinez from the FENTOM group at INGAR for providing us with the magnetite nanoparticles his group synthesized, Dr. Guillermo Zampieri for allowing us to perform these experiments in his laboratory at Centro Atómico Bariloche, as well as for his useful insights, and Dra. Silvia Montoro and Dra. Lucila Cristina for the help performing the measurements. This work was funded by ANPCyT via the project PICT-RAICES 2013-0164.

Supplementary materials

Supplementary material associated with this article can be found, in the online version, at doi:10.1016/j.susc.2017.10.009.

References

[1] B. Hapke, Space weathering from Mercury to the asteroid belt, J. Geophys. Res. 106 (2001) 10039.
[2] R. Brunetto, G. Strazzulla, Elastic collisions in ion irradiation experiments: A mechanism for space weathering of silicates, Icarus 179 (2005) 265.
[3] G. Wächtershäuser, On the chemistry and evolution of the pioneer organism, Chem. Biodivers. 4 (2007) 584.
[4] T. Burbine, R.P. Binzel, Small Main-Belt Asteroid Spectroscopic Survey in the Near-Infrared, Icarus 159 (2002) 468.
[5] C.T. Pillinger, Solar-wind exposure effects in the lunar soil, Reports Prog. Phys. 42 (2001) 897.
[6] B. Hapke, Darkening of silicate rock powders by solar wind sputtering, Moon 7 (1973) 342.
[7] D.T. Rickard, Pyrite : A Natural History of Fool's Gold, Oxford University press, 2015.
[8] C.A. Dukes, R.A. Baragiola, L.A. McFadden, Surface modification of olivine by H+ and He+ bombardment, J. Geophys. Res. 104 (1999) 1865.
[9] S. Garaj, W. Hubbard, J.A. Golovchenko, Graphene synthesis by ion implantation, Appl. Phys. Lett. 97 (2010) 183103.
[10] L. Cristina, L. Gomez, R. Vidal, J. Ferron, Diffusion of implanted nitrogen in the Cu(001) surface, J. Phys. D-Applied Phys. 43 (2010) 185302.
[11] L.J. Cristina, J.C. Moreno-López, S.J. Sferco, M.C.G. Passeggi, R.A. Vidal, J. Ferrón, Surface characterization of self-assembled N-Cu nanostructures, Appl. Surf. Sci. 258 (2012) 2047.
[12] F.M. Leibsle, Nanostructure fabrication on copper surfaces, Surf. Sci. 514 (2002) 33.
[13] F.M. Leibsle, C.F.J. Flipse, A.W. Robinson, Structure of the Cu{100}- c (2×2)N surface: A scanning-tunneling-microscopy study, Phys. Rev. B 47 (1993) 15865.
[14] G. Wächtershäuser, Pyrite Formation, the First Energy Source for Life: a Hypothesis, Syst. Appl. Microbiol. 10 (1988) 207.

[15] M.J. Russell, W. Martin, The rocky roots of the acetyl-CoA pathway, Trends Biochem. Sci. 29 (2004) 358.
[16] L. Ding, X. Fan, X. Sun, J. Du, Z. Liu, C. Tao, Direct preparation of semiconductor iron sulfide nanocrystals from natural pyrite, RSC Adv 3 (2013) 4539.
[17] K.M. Rosso, U. Becker, M.F. Hochella, The interaction of pyrite {100} surfaces with O_2 and H_2O: Fundamental oxidation mechanisms, Am. Mineral. 84 (1999) 1535.
[18] K. Andersson, M. Nyberg, H. Ogasawara, D. Nordlund, T. Kendelewicz, C.S. Doyle, G.E. Brown, L.G.M. Pettersson, A. Nilsson, Experimental and theoretical characterization of the structure of defects at the pyrite FeS_2(100) surface, Phys. Rev. B 70 (2004) 195404.
[19] S. Chaturvedi, R. Katz, J. Guevremont, M.A.A. Schoonen, D.R. Strongin, XPS and LEED study of a single-crystal surface of pyrite, Am. Mineral. 81 (1996) 261.
[20] T. Tsang, G.J. Coyle, I. Adler, L. Yin, XPS studies of ion bombardment damage of iron—sulfur compounds, J. Electron Spectros. Relat. Phenomena 16 (1979) 389–396.
[21] M. Sanchez-Arenillas, E. Mateo-Marti, Pyrite surface environment drives molecular adsorption: cystine on pyrite(100) investigated by X-ray photoemission spectroscopy and low energy electron diffraction, Phys. Chem. Chem. Phys. 18 (2016) 27219.
[22] V. Yathindranath, L. Rebbouh, D.F. Moore, D.W. Miller, J. van Lierop, T. Hegmann, A Versatile Method for the Reductive, One-Pot Synthesis of Bare, Hydrophilic and Hydrophobic Magnetite Nanoparticles, Adv. Funct. Mater. 21 (2011) 1457.
[23] J.J. Joyce, M. Del Giudice, J.H. Weaver, Quantitative analysis of synchrotron radiation photoemission core level data, J. Electron Spectros. Relat. Phenom. 49 (1989) 31.
[24] M.C. Biesinger, B.P. Payne, A.P. Grosvenor, L.W.M. Lau, A.R. Gerson, R.S.C. Smart, Resolving surface chemical states in XPS analysis of first row transition metals, oxides and hydroxides: Cr, Mn, Fe, Co and Ni, Appl. Surf. Sci. 257 (2011) 2717.
[25] H.W. Nesbitt, M. Scaini, H. Höchst, G.M. Bancroft, A.G. Schaufuss, R. Szargan, Synchrotron XPS evidence for Fe2+-S and Fe3+-S surface species on pyrite fracture–surfaces, and their 3D electronic states, Am. Mineral. 85 (2000) 850.
[26] E.R. Malinowski, D.G. Howery, Factor Analysis in Chemistry, Wiley, New York, 1980.
[27] N. Moslemzadeh, M. Tamara, R. Raval, D. Prior, M.R. Preston, Improved efficiency of the sputtering technique for pyrite surface and its effect on reduction of electron beam damage, Surf. Interface Anal. 41 (2009) 1.
[28] A.N. Buckley, R. Woods, The surface oxidation of pyrite, Appl. Surf. Sci. 27 (1987) 437.
[29] S. Karthe, R. Szargan, E. Suoninen, Oxidation of pyrite surfaces: a photoelectron spectroscopic study, Appl. Surf. Sci. 72 (1993) 157.
[30] H.W. Nesbitt, I.J. Muir, X-ray photoelectron spectroscopic study of a pristine pyrite surface reacted with water vapour and air, Geochim. Cosmochim. Acta 58 (1994) 4667.
[31] S.W. Knipe, J.R. Mycroft, A.R. Pratt, H.W. Nesbitt, G.M. Bancroft, X-ray photoelectron spectroscopic study of water adsorption on iron sulfide minerals, Geochim. Cosmochim. Acta 59 (1995) 1079.
[32] C.M. Eggleston, J.-J. Ehrhardt, W. Stumm, Surface structural controls on pyrite oxidation kinetics: An XPS-UPS, STM, and modeling study, Am. Mineral. 81 (1996) 1036.
[33] A.G. Schaufuss, H.W. Nesbitt, I. Kartio, K. Laajalchto, G.M. Bancroft, R. Szargan, Reactivity of surface chemical states on fractured pyrite, Surf. Sci. 411 (1998) 321.
[34] A.G. Schaufuss, H.W. Nesbitt, I. Kartio, K. Laajalchto, G.M. Bancroft, R. Szargan, Incipient oxidation of fractured pyrite surfaces in air, J. Electron Spectros. Relat. Phenom. 96 (1998) 69.
[35] H.W. Nesbitt, G.M. Bancroft, A.R. Pratt, A.M.J. Scaini, Sulfur and iron surface states on fractured pyrite surfaces, Am. Mineral. 83 (1998) 1067.
[36] N.S. McIntyre, D.G. Zetaruk, X-ray photoelectron spectroscopic studies of iron oxides, Anal. Chem. 49 (1977) 1521.
[37] J.R. Mycroft, G.M. Bancroft, N.S. McIntyre, L.W. Lorimer, I.R. Hill, Detection of sulphur and polysulphides on electrochemically oxidized pyrite surfaces by X-ray photoelec tron spectroscopy and Raman spectroscopy, J. Electroanlitic Chem 292 (1990) 139.
[38] C.J. Powell, A. Jablonski, NIST Electron Inelastic-Mean-Free-Path Database, National Institute of Standards and Technology, Gaithersburg, MD, 2010.
[39] J.F. Ziegler, M.D. Ziegler, J.P. Biersack, SRIM - The stopping and range of ions in matter, Nucl. Instrum. Methods Phys. Res. Sect. B Beam Interact. Mater. Atoms 268 (2010) 1818.
[40] J.E. Thomas, W.M. Skinner, R.St.C. Smart, A comparison of the dissolution behavior of troilite with other iron (II) sulfides; implications of structure, Geochim. Cosmochim. Acta 67 (2003) 831.
[41] J. Leveneur, G.I.N. Waterhouse, J. Kennedy, J.B. Metson, D.R.G. Mitchell, Nucleation and growth of Fe nanoparticles in SiO_2: A TEM, XPS, and Fe L-Edge XANES investigation, J. Phys. Chem. C 115 (2011) 20978.
[42] J.F. Moulder, W.F. Stickle, P.E. Sobol, K.D. Bomben, Handbook of X-ray Photoelectron Spectroscopy, 2nd ed., Perkin-Elmer Corp., Physical Electronics Division, Eden Prairie, Minnesota, USA, 1992.